ABSTRACT

YAXING LIU. Use of the Thin-Strut FDTD Formalism For the Design of Coils In Biomedical Telemetry Applications. (Under the direction of Dr. Gianluca Lazzi.)

For many years, inductively coupled telemetry systems have been designed and used for transcutaneous energy transfer in biomedical applications. But most of these designs are mainly based on steady state circuit analysis. To our knowledge, no specific computational electromagnetic techniques have been developed to analyze the coupled systems. This thesis extends the thin-strut FDTD formalism to study the coupling of an external primary coil and an implanted secondary coil in the biomedical telemetry applications. The stability and convergence analyses are discussed, from the unconditionally stable semi-discrete field-wire system to the conditionally stable fully-discrete system. A new stability criterion for selecting the time step is introduced. Computational experiments demonstrate the effectiveness and the accuracy of this extension, provided that the time step is properly chosen.

Keywords: FDTD method, thin-strut FDTD formalism, stability, convergence, semi-discrete system, fully-discrete system, Von Neumann stability analysis, Courant stability limit.

USE OF THE THIN-STRUT FDTD FORMALISM FOR THE DESIGN OF COILS IN BIOMEDICAL TELEMETRY APPLICATIONS

by

YAXING LIU

A thesis submitted to the Graduate Faculty of
North Carolina State University
in partial fulfillment of the
requirements for the Degree of
Master of Science

ELECTRICAL ENGINEERING

Raleigh

2003

APPROVED BY:

Chair of Advisory Committee

To dear Mom and Dad

BIOGRAPHY

Yaxing Liu was born in Anqing, Anhui, P.R. China in 1978. After she got her Bachelor's degree in electrical engineering from University of Science & Technology of China in 2000, she joined NC State University in Fall 2000 in electrical engineering as a research assistant under the guidance of Dr. Gianluca Lazzi. Since then, she was working in the application of computational electromagnetics and smart telemetry systems to the development of a retinal prosthesis to restore the sight in the blind. Her research interests include numerical electromagnetics, bioelectromagnetics, computer aided design of nonlinear circuits, remote sensing, and microwave optical interactions.

ACKNOWLEDGEMENTS

I would like to take this opportunity to thank all those people without whom I would not have been able to realize my Master's degree and this thesis in particular.

I would like to give my sincerest thanks to my advisor, Dr. Gianluca Lazzi for his help, stimulating suggestions, and encouragement in all the time researching and writing this thesis. He has been an excellent guide, a very considerate supervisor, and his enthusiasm about work is extremely contagious. I have been deeply impressed by his ability to respond to various work and non-work related situations with sensitivity and understanding. I thoroughly enjoyed the learning and the research experience during these two years.

Special thanks also to my committee members, Dr. Zhilin Li and Dr. Michael Steer, for their enthusiastic involvement and constructive help throughout. I would especially like to thank Dr. Zhilin Li for many critical discussions and helpful comments he has provided pertinent to my research.

It has been my privilege to have been on the receiving end of the help, support, advice and friendship of many colleagues (past and present) including, Arvind Venugopal, Chris Demarco, Michael Edward Eberdt, Keyoor Gosalia, Stefan Schmidt, Anand S. Konanur, Patrick Kelly Brown, and Abheek Gupta.

Last and most important, I wish to express my deepest thanks to my parents who formed part of my vision and taught me the things that really matter in life. I thank them for having faith in me and always encouraging me through letters and calls.

Contents

List of Figures

List of Tables

Chapter 1

Introduction

1.1 Biomedical Inductively Coupled Telemetry Systems

Inductively coupled telemetry systems have been in use in a wide range of biomedical applications, including pacemaker, cardiac assistance and replacement devices, as well as in cochlear, visual or urinary prosthesis. To avoid the possibility of infection by wires piercing the skin and the undesirable replacement of the implanted power source, power to energize the implanted devices is provided outside the body transcutaneously. These systems usually consist of an external primary coil and an implanted secondary coil separated by a layer of skin and tissues. Their magnetic link allows energy transfer through the biological tissue from the transmitter to the implant using frequencies generally lower than $10MHz$ [1].

Because of skin mobility and variations in thickness of subcutaneous fatty tissue, lateral and angular misalignments of the coils easily occur, leading to a change of transmission characteristics. There have been several analyses and approaches to the design of magnetic transcutaneous links [2]-[5] which take into account the misalignments and their effects on coupling efficient. Donaldson and Perkins [2] demonstrated the advantage of operating the coils near critical coupling and explained design tradeoffs, such as efficiency and misalignment tolerances. Galbraith *et al.* [3] described a method of desensitizing the

link gain by stagger tuning the transmitter and receiver circuits off the operating frequency. Flack *et al.* [5] provided computer-derived graphs for the lateral misalignment case. Almost all of these designs relied mainly on steady-state circuit analysis, the experimental work by Terman [8], and trial-and-error techniques for each particular case. To our knowledge, no specific numeric computational electromagnetic techniques have been developed for the analysis of coupled coils in transcutaneous telemetry applications.

1.2 Computational Electromagnetics

With the relentless advances in computational efficiency and increases in memory capacity, a number of analytical and numerical approaches for the solutions of Maxwell's equations are widely used. Computational electromagnetic methods have been applied to study the radiation, scattering and penetration of electromagnetic wave with three-dimensional objects, in problems related to telecommunication, EM compatibility, microwave devices and guiding structures, medical diagnosis and therapy. Among these numerical algorithms, there are two main classes of methods: the frequency-domain integro-differential equation approach via the Method of Moments (MOM), the time-domain differential-equation approach via the Finite-Difference Time-Domain (FDTD) method and the Finite Element method (FE).

When deciding to choose the most suitable numerical technique to solve a particular problem, many factors have to be taken into account, including the geometry of the scattering and radiating objects, computer requirements, frequency-domain or time-domain, and radiation boundary conditions. The geometry and the material characteristics of the object of interest play important roles in selecting the approach used to model its electromagnetic interaction properties. In biomedical applications, the object is such an inhomogeneous, irregular, penetrable body that it can not be easily included in the MOM formulations. However, the powerful ability of FDTD to analyze inhomogeneous materials makes the FDTD method very attractive.

1.3 Numerical Method FDTD

First introduced by Yee [9], FDTD is widely used to solve electromagnetic problems because of its many attractive features, including:

- Simplicity: It directly uses second-order accurate central finite difference approximations for the temporal and spatial derivatives of the electric and magnetic fields to explicitly solve Maxwell's time-dependent curl equations with no linear algebra used;

- Effectiveness: Because FDTD is a marching-in-time procedure performed in the time-domain, it can obtain a broad band response with a single simulation by the Fourier Transform postprocessing; Moreover, problems that involve nonlinear media or components can usually be easily solved in a more straightforward and efficient manner in the time-domain, compared with those in the frequency-domain.

- Robustness: Numerical dispersions in FDTD calculations are well understood and can be bounded to accurately model a very large variety of electromagnetic wave interaction problems.

- Versatility: It can inherently model highly inhomogenous materials such as biological tissues, geophysical strata, and reentrant or shielding metal structures. Moreover, because in FDTD the new value of a field vector component at any lattice point depends only on its previous value, and on the previous values of the components of the other field vector at adjacent points, the computation of a field vector can proceed either one point at a time or several points concurrently. Parallelized FDTD is especially useful for extremely large models.

More details of the FDTD's features will be explained in Section 2.2.3.

1.4 Modified FDTD For Small Features of Scattering Objects

Although the standard FDTD method has the advantages mentioned above, it is not well suited for modelling accurately small geometric details like thin wires and strips which are essential structures in biomedical telemetry coil design. The most straightforward approach to include wires into the FDTD computational grid is to model the thin wire as a perfect electric conductor by setting all the tangential electric field components on the wire surface equal to zero. This is generally adequate for wires of radius comparable to the cell size. However, as for thin wires with cross-sections that are very small relative to the problem space, a very high resolution grid is necessary in order to accurately model the wire. For the standard FDTD method with a uniform grid, high resolution will generally result in a large number of cells, and excessive computer memory and longer run time.

Therefore, many modified FDTD formalisms have been proposed to model these small but important structural features while maintaining the simulation feasible.

In [10]-[12], sub-gridding methods have been proposed, in which some subdomains were gridded more finely than the rest of the FDTD problem space. However, they presented potential problems concerning stability and accuracy of the coupling between the fine and coarse meshes.

Alternatively, the thin-wire subcell FDTD models [14]–[15] included the effects of a wire by modifying the updating formulas for the electromagnetic fields near the wire. There are two main FDTD subcell models: the Faraday's law contour-path model proposed by Umashankar *et al.* [13] and the in-cell equivalent inductance model proposed by Holland *et al.* [14].

Umashankar *et al.* included the effect of wires directly into the stencil of Yee's scheme with the Faraday's law contour integral approach to model the electromagnetic fields near the wire, assuming that the circumferential component of the magnetic field and the radial component of the electric field vary as $1/r$ near the wire, where r is the radial distance from the wire axis.

On the other hand, the thin-strut FDTD formalism proposed by Holland *et al.* separated wires from the three-dimensional volume and solved two mutually interacting problems by introducing an "in-cell inductance" model of wires and solving the simultaneous, coupled equations for the currents and the charge densities concurrently with the FDTD time stepping.

In this thesis we extend Holland's method to model the coupling between primary and secondary coils in biomedical telemetry systems. Results are compared with those obtained by the quasi-static analysis, the conventional FDTD method, and the well-known method of moments (MOM) based code—the Numerical Electromagnetic Code (NEC) [6]. The thin-strut FDTD formalism and the perfectly matched layer (PML) absorbing boundary condition [7] have been applied to calculate the current ratio of the inductively link system with different external coils. Stability and convergence of the thin-strut FDTD formalism are also discussed. Results illustrate that thin-strut FDTD is more accurate than the conventional FDTD for the considered problem.

1.5 Overview of Thesis

Chapter 2 reviews the FDTD technique starting from Yee's finite difference formulation of Maxwell's curl equations to form the necessary theoretical foundation for later chapters. Chapter 3 describes the analytical design of coils in telemetry systems. The use of the thin-strut FDTD formalism by Holland *et al.* [14] for the numerical analysis of coupled coils is described in Chapter 4. A detailed analysis of the stability and convergence problems in the modified FDTD method are presented and a new stability criterion is introduced. Results for different configurations of telemetry systems demonstrate the effectiveness and the accuracy of our extension of the thin-strut FDTD formalism. Chapter 5 discusses the conclusions and future work.

Chapter 2

Governing Equations and FDTD

2.1 Maxwell's Equations

Electromagnetic phenomena are described by Maxwell's equations:

$$\textit{Faraday's Law}: \quad \nabla \times \boldsymbol{E} = -\frac{\partial \boldsymbol{B}}{\partial t} + \boldsymbol{M} \tag{2.1}$$

$$\textit{Ampere's Law}: \quad \nabla \times \boldsymbol{H} = \frac{\partial \boldsymbol{D}}{\partial t} + \boldsymbol{J} \tag{2.2}$$

$$\textit{Gauss's Law}: \quad \nabla \cdot \boldsymbol{D} = \rho \tag{2.3}$$

$$\textit{Gauss's Law}: \quad \nabla \cdot \boldsymbol{B} = 0 \tag{2.4}$$

where

$\boldsymbol{E}$ is the electric field $[V/m]$,

$\boldsymbol{H}$ is the magnetic field $[A/m]$,

$\boldsymbol{D}$ is the electric flux density $[C/m^2]$,

$\boldsymbol{B}$ is the magnetic flux density $[Wb/m^2]$,

$\boldsymbol{J}$ is the electric current density $[A/m^2]$,

$\boldsymbol{M}$ is the equivalent magnetic current density$[V/m^2]$,

ρ is the charge density $[C/m^3]$.

The introduction of the equivalent magnetic current density increases the symmetry of Maxwell's equations. This term can also be included in the FDTD method. Moreover,

the four Maxwell's equations are complemented by the equation of continuity,

$$\nabla \cdot \boldsymbol{J} = -\frac{\partial \rho}{\partial t} \ . \tag{2.5}$$

By taking the divergence on the Ampere's and Faraday's laws, the two divergence equations can be derived from the two curl equations and the equation of continuity .

For linear, isotropic and non-dispersive materials, we have two constitutive equations:

$$\boldsymbol{B} = \mu \boldsymbol{H} \tag{2.6}$$

$$\boldsymbol{D} = \epsilon \boldsymbol{E} \tag{2.7}$$

where ϵ is the permittivity and μ is the permeability of the material.

Moreover, if we allow for materials with isotropic, non-dispersive electric and magnetic losses that attenuate E fields via conversion to heat energy, we have

$$\boldsymbol{J} = \sigma \boldsymbol{E} \tag{2.8}$$

$$\boldsymbol{M} = \sigma^* \boldsymbol{H} \tag{2.9}$$

where

σ is the electric conductivity $[S/m]$,

σ^* is the equivalent magnetic loss $[\Omega/m]$.

The vector components of the curl operators of Equation (2.1) and (2.2) represent a system of six scalar equations which can be expressed in Cartesian coordinates as:

$$
\begin{aligned}
\frac{\partial E_x}{\partial t} &= \frac{1}{\epsilon}\left(\frac{\partial H_z}{\partial y} - \frac{\partial H_y}{\partial z} - \sigma E_x\right) \\
\frac{\partial E_y}{\partial t} &= \frac{1}{\epsilon}\left(\frac{\partial H_x}{\partial z} - \frac{\partial H_z}{\partial x} - \sigma E_y\right) \\
\frac{\partial E_z}{\partial t} &= \frac{1}{\epsilon}\left(\frac{\partial H_y}{\partial x} - \frac{\partial H_x}{\partial y} - \sigma E_z\right) \\
\frac{\partial H_x}{\partial t} &= \frac{1}{\mu}\left(\frac{\partial E_y}{\partial z} - \frac{\partial H_z}{\partial y} - \sigma^* H_x\right) \\
\frac{\partial H_y}{\partial t} &= \frac{1}{\mu}\left(\frac{\partial E_z}{\partial x} - \frac{\partial H_x}{\partial z} - \sigma^* H_y\right) \\
\frac{\partial H_z}{\partial t} &= \frac{1}{\mu}\left(\frac{\partial E_x}{\partial y} - \frac{\partial H_y}{\partial x} - \sigma^* H_z\right)
\end{aligned}
\tag{2.10}
$$

According to the definition of hyperbolic equations in [16], Maxwell's equations is a first order hyperbolic system because all eigenvalues are real.

2.2 The FDTD Formulation

2.2.1 Introduction

The finite-difference time-domain (FDTD) method, originally proposed by Yee in 1966 [9] and later developed by Taflove *et al.* [18] provides a direct solution to Maxwell's curl equations (2.1) and (2.2). Because of its simplicity and computational efficiency, it is one of the most popular numerical methods for the solution of electromagnetic problems. Although the FDTD method has existed for over thirty years, its popularity continues to grow as computing costs continue to decline. It has been used to solve a large number of applications in electromagnetics, such as electromagnetic scattering, electromagnetic pulse (EMP) simulation, EMC/EMI, bio-electromagnetic (hyperthermia, MRI, bio-hazards), antenna modelling in telecommunication, microwave circuit devices and systems, electronic packaging, and non-linear optics. In addition, extensions and enhancements to the FDTD method are continually being published, which further broadens

its usefulness [21].

In the FDTD method, the temporal and spatial derivatives are approximated by the second order accurate central difference equations. Therefore, the set of partial differential equations is transformed into a system of algebraic equations where derivatives are replaced by finite differences. The computational region is divided into cells and the components of the $\boldsymbol{E}$ and $\boldsymbol{H}$ fields are placed on the mesh as shown in the Figure 2.1, with the magnetic fields displaced by a half a cell distance from the electric fields.

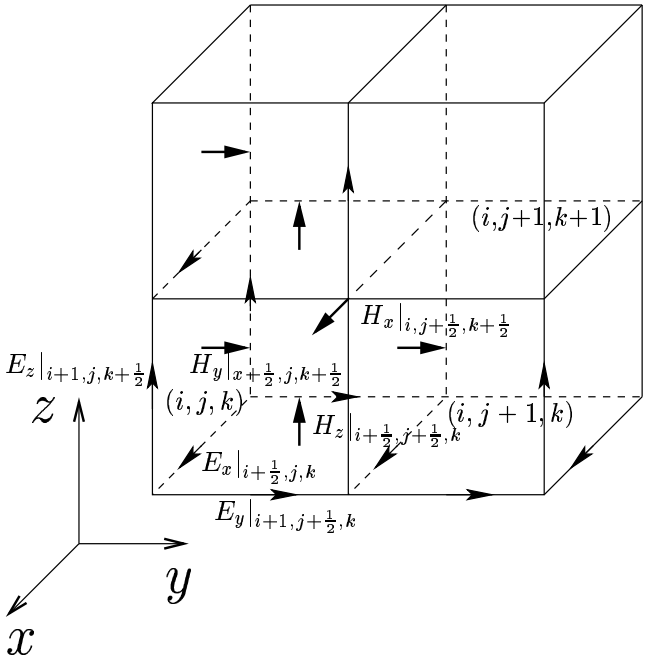

Figure 2.1: FDTD grid.

Note that each electric field vector component is surrounded by four circulating magnetic field vector components, and vise versa. This arrangement permits easy implementations of central finite difference approximations and the integral form of the Faraday's law and the Ampere's law. The system of difference equations is solved at the nodes. The field quantities are solved with a "leap-frog" scheme where a half time step separates the solutions of the electric and magnetic fields. Time-stepping is continued until the desired late-time pulse response or steady state behavior is observed.

2.2.2 Discretization and Modeling In FDTD

Following Yee's notation [9], we define a grid point in a uninform rectangular lattice as:

$$(i, j, k) = (i\Delta x, j\Delta y, k\Delta z) \tag{2.11}$$

where Δx, Δy, and Δz are, respectively, the spatial increments in the x, y, and z directions, and i, j, and k are integers. Further, we define any function f of space and time evaluated at a discrete point in the grid and at a discrete point in time as:

$$f|^n_{i,j,k} = f(i\Delta x, j\Delta y, k\Delta z, n\Delta t) \tag{2.12}$$

where Δt is the time increment, assumed uniform over the observation interval and n is an integer.

Taking the central finite difference approximations for both temporal and spatial derivatives of f gives,

$$\frac{\partial f|^n_{i,j,k}}{\partial t} = \frac{f|^{n+\frac{1}{2}}_{i,j,k} - f|^{n-\frac{1}{2}}_{i,j,k}}{\Delta t} + O\left[(\Delta t)^2\right] \tag{2.13}$$

$$\frac{\partial f|^n_{i,j,k}}{\partial x} = \frac{f|^n_{i+\frac{1}{2},j,k} - f|^n_{i-\frac{1}{2},j,k}}{\Delta x} + O\left[(\Delta x)^2\right] \tag{2.14}$$

2.2.3 Updating Stencils For FDTD

In homogeneous materials with $\sigma^* = 0$, the following system equations comprise the FDTD updating stencils for the electromagnetic field components.

$$\boldsymbol{H}_x|^{n+\frac{1}{2}}_{i,j+\frac{1}{2},k+\frac{1}{2}} = \boldsymbol{H}_x|^{n-\frac{1}{2}}_{i,j+\frac{1}{2},k+\frac{1}{2}} + \frac{\Delta t}{\mu}\left[\frac{\dfrac{\boldsymbol{E}_y|^n_{i,j+\frac{1}{2},k+1} - \boldsymbol{E}_y|^n_{i,j+\frac{1}{2},k}}{\Delta z} - \dfrac{\boldsymbol{E}_z|^n_{i,j+1,k+\frac{1}{2}} - \boldsymbol{E}_z|^n_{i,j,k+\frac{1}{2}}}{\Delta y}}{}\right] \tag{2.15}$$

$$\boldsymbol{H}_y|^{n+\frac{1}{2}}_{i+\frac{1}{2},j,k+\frac{1}{2}} = \boldsymbol{H}_y|^{n-\frac{1}{2}}_{i+\frac{1}{2},j,k+\frac{1}{2}} + \frac{\Delta t}{\mu}\left[\frac{\dfrac{\boldsymbol{E}_z|^n_{i+1,j,k+\frac{1}{2}} - \boldsymbol{E}_z|^n_{i,j,k+\frac{1}{2}}}{\Delta x} - \dfrac{\boldsymbol{E}_x|^n_{i+\frac{1}{2},j,k+1} - \boldsymbol{E}_x|^n_{i+\frac{1}{2},j,k}}{\Delta z}}{}\right] \tag{2.16}$$

$$\boldsymbol{H}_z\big|_{i+\frac{1}{2},j+\frac{1}{2},k}^{n+\frac{1}{2}} = \boldsymbol{H}_z\big|_{i+\frac{1}{2},j+\frac{1}{2},k}^{n-\frac{1}{2}} + \frac{\Delta t}{\mu}\left[\begin{array}{c}\dfrac{\boldsymbol{E}_x\big|_{i+\frac{1}{2},j+1,k}^{n} - \boldsymbol{E}_x\big|_{i+\frac{1}{2},j,k}^{n}}{\Delta y} - \\ \dfrac{\boldsymbol{E}_y\big|_{i+1,j+\frac{1}{2},k}^{n} - \boldsymbol{E}_y\big|_{i,j+\frac{1}{2},k}^{n}}{\Delta x}\end{array}\right] \tag{2.17}$$

$$\begin{aligned}\boldsymbol{E}_x\big|_{i+\frac{1}{2},j,k}^{n+1} = {} & \left(\frac{1-\dfrac{\sigma\Delta t}{2\epsilon}}{1+\dfrac{\sigma\Delta t}{2\epsilon}}\right)\boldsymbol{E}_x\big|_{i+\frac{1}{2},j,k}^{n} + \\ & + \left(\frac{\dfrac{\Delta t}{\epsilon}}{1+\dfrac{\sigma\Delta t}{2\epsilon}}\right)\left[\begin{array}{c}\dfrac{\boldsymbol{H}_z\big|_{i+\frac{1}{2},j+\frac{1}{2},k}^{n+\frac{1}{2}} - \boldsymbol{H}_z\big|_{i+\frac{1}{2},j-\frac{1}{2},k}^{n+\frac{1}{2}}}{\Delta y} - \\ \dfrac{\boldsymbol{H}_y\big|_{i+\frac{1}{2},j,k+\frac{1}{2}}^{n+\frac{1}{2}} - \boldsymbol{H}_y\big|_{i+\frac{1}{2},j,k-\frac{1}{2}}^{n+\frac{1}{2}}}{\Delta z}\end{array}\right]\end{aligned} \tag{2.18}$$

$$\begin{aligned}\boldsymbol{E}_y\big|_{i,j+\frac{1}{2},k}^{n+1} = {} & \left(\frac{1-\dfrac{\sigma\Delta t}{2\epsilon}}{1+\dfrac{\sigma\Delta t}{2\epsilon}}\right)\boldsymbol{E}_y\big|_{i,j+\frac{1}{2},k}^{n} + \\ & + \left(\frac{\dfrac{\Delta t}{\epsilon}}{1+\dfrac{\sigma\Delta t}{2\epsilon}}\right)\left[\begin{array}{c}\dfrac{\boldsymbol{H}_x\big|_{i,j+\frac{1}{2},k+\frac{1}{2}}^{n+\frac{1}{2}} - \boldsymbol{H}_x\big|_{i,j+\frac{1}{2},k-\frac{1}{2}}^{n+\frac{1}{2}}}{\Delta z} - \\ \dfrac{\boldsymbol{H}_z\big|_{i+\frac{1}{2},j+\frac{1}{2},k}^{n+\frac{1}{2}} - \boldsymbol{H}_z\big|_{i-\frac{1}{2},j+\frac{1}{2},k}^{n+\frac{1}{2}}}{\Delta x}\end{array}\right]\end{aligned} \tag{2.19}$$

$$\begin{aligned}\boldsymbol{E}_z\big|_{i,j,k+\frac{1}{2}}^{n+1} = {} & \left(\frac{1-\dfrac{\sigma\Delta t}{2\epsilon}}{1+\dfrac{\sigma\Delta t}{2\epsilon}}\right)\boldsymbol{E}_z\big|_{i,j,k+\frac{1}{2}}^{n} + \\ & + \left(\frac{\dfrac{\Delta t}{\epsilon}}{1+\dfrac{\sigma\Delta t}{2\epsilon}}\right)\left[\begin{array}{c}\dfrac{\boldsymbol{H}_y\big|_{i+\frac{1}{2},j,k+\frac{1}{2}}^{n+\frac{1}{2}} - \boldsymbol{H}_y\big|_{i-\frac{1}{2},j,k+\frac{1}{2}}^{n+\frac{1}{2}}}{\Delta x} - \\ \dfrac{\boldsymbol{H}_x\big|_{i,j+\frac{1}{2},k+\frac{1}{2}}^{n+\frac{1}{2}} - \boldsymbol{H}_x\big|_{i,j-\frac{1}{2},k+\frac{1}{2}}^{n+\frac{1}{2}}}{\Delta y}\end{array}\right]\end{aligned} \tag{2.20}$$

Note that the constitutive parameters of each material type that exists in the FDTD space are interpreted by the FDTD program as local coefficients for the time-stepping algorithm. The material parameters are calculated and stored before time stepping begins. Since the material which interacts with each field component is specified separately,

material modelling is straightforward in the FDTD method.

For inhomogeneous materials, we replace the constitutive parameters in updating equations with the constitutive parameters of the corresponding cell. For example, for the cell (i, j, k), ϵ in Equation (2.18) will be substituted by $\epsilon_{i+\frac{1}{2},j,k}$, and similarly for σ.

For frequency-dependent media, we can use the frequency-dependent FDTD method to get a broad band result. It is more efficient than using a sequence of single frequency FDTD simulations. The Debye equation and Lorentz form [20] are the alternatives to describe the complex permittivity of dispersive materials by an equation with one or more second order poles.

2.2.4 Sources

Proper modelling of sources is essential in all FDTD applications. For the FDTD simulations with internal sources, we can excite the simulation with a "hard" or "soft" source [24]. The "hard" source is implemented by specifying the field at a given node with a temporal driving function. The "soft" source is achieved by adding the source function to the FDTD calculated values. With the use of a pulse source in the time-domain and the Fourier Transformation, a single FDTD simulation can provide results over a broad frequency range.

2.2.5 Two-Equations Two-Unknowns Method

Traditionally, a peak detection method or a Fourier Transform method is used to convert the result from the time-domain to the frequency-domain for analyzing steady state frequency-domain behavior. In that condition, the simulation should be run for a full cycle past convergence which requires a large amount of computer time and memory, especially for low frequencies and high resolutions. In [22]-[23], a simple and direct method to obtain the magnitude and the phase of a sinusoidal wave in the time-domain has been proposed.

Following [22], at all locations in space, at two separate time steps t_1 and t_2, for a

problem characterized by a clean sinusoidal wave output, we have

$$A\sin(\omega t_1+\theta) = q_1 \tag{2.21}$$

$$A\sin(\omega t_2+\theta) = q_2 \tag{2.22}$$

where A is the magnitude, θ is the phase angle, ω is the angular frequency.

Therefore, the amplitude A and the phase θ can be derived once q_1 and q_2 are known by using:

$$\theta = \arctan\left[\frac{q_2\sin(\omega t_1)-q_1\sin(\omega t_2)}{q_1\cos(\omega t_2)-q_2\cos(\omega t_1)}\right] \tag{2.23}$$

$$A = \left|\frac{q_2}{\sin(\omega t_2+\theta)}\right| \tag{2.24}$$

In order to avoid the numerical round-off errors, especially in the high resolution simulations, it is desirable to choose t_1 and t_2 to be not contiguous, but still select them within one fourth of the whole wave period. Ramped-sine excitations can be used to reduce or eliminate numerical noises.

2.2.6 FDTD Absorbing Boundary Conditions

For the case of an unbounded problem, a separate numerical absorbing boundary condition (ABC) at the edges of a finite mesh is employed to truncate the computational region. There have been numerous ABC approaches [24] to effectively approximate an infinite mesh.

One of the most flexible and efficient methods is the perfectly matched layer (PML) developed by Bérenger [19]. The basic idea is to produce an artificial lossy medium by complex ϵ and μ so that the wave will be absorbed before it hits the boundary. Details about PML implementations are available in [24] and will not be discussed here for brevity.

2.2.7 Numerical Dispersion and Stability

To ensure the FDTD numerical accuracy, the spatial increment h used in the simulation is required to be small enough compared to the wavelength. Usually, as [24] suggests,

$h \leq \lambda_{min}/10$, where λ_{min} is the shortest wavelength at the frequency of computation.

On the other hand, to ensure the stability of the computation process, the time increment Δt must satisfy the CFL (Courant-Friedrich-Lövy) criterion [24],

$$\Delta t \leq \frac{1}{c\sqrt{\frac{1}{(\Delta x)^2} + \frac{1}{(\Delta y)^2} + \frac{1}{(\Delta z)^2}}} = \frac{h}{\sqrt{3}c}, \tag{2.25}$$

where $\Delta x = \Delta y = \Delta z = h$ for the three-dimensional cubic-cell space lattice. In general, to ensure stability the time step is bounded by

$$\Delta t \leq \frac{h}{c\sqrt{n}}, \tag{2.26}$$

where n is the number of space dimensions.

Chapter 3

Analytical Design of Biomedical Telemetry Systems

3.1 Introduction

Magnetic transcutaneous coupling of power to implanted electronic devices is preferred over other alternatives for many implanted biomedical electronic systems. The development of a telemetry system needs a high-efficiency magnetic link. Mutual inductance between the external primary coil and the implanted secondary coil is a quantitative description of the flux coupling and inductive link.

Since we are mainly concerned with biomedical telemetry systems, many other factors have to be taken into account, such as size and shape of the coils, location of the implant, misalignment tolerance and overall efficiency of the power transfer to the load. Each application has its own unique requirements which affects the priority of these factors. There exists considerable knowledge on the circuit design of such links and practical examples have been described in the literature [2]-[5].

In this chapter, we first use the magnetic vector potential to calculate the mutual inductance between two parallel coils as a quasi-static problem. It is used first for circular coils and then for square coils. The results of this quasi-static analysis are in good agreement with the Terman's formula which was based mainly on experimental work [8]. Then we summarize the tradeoff in the system design and state the reason why we choose

current ratio as our design benchmark.

3.2 Mutual Inductance

3.2.1 Definition

Magnetic coupling between coils is often used for transmitting power and data into devices implanted in the body. Mutual inductance describes the coupling of two coils via a magnetic field. The mutual inductance M_{12} of coil 2 in relation to coil 1 is defined as the ratio of the mutual magnetic flux linkage Ψ_{12} enclosed by coil 2, to the current I_1 in coil 1, see [17]. The most direct approach is to use the magnetic flux density from the Biot-Savart law:

$$M_{12} = \frac{\Psi_{12}}{I_1} = \frac{\int_{S_2} \boldsymbol{B}_1 \cdot d\boldsymbol{s}_2}{I_1}, \tag{3.1}$$

where $\boldsymbol{B}_1$ is the magnetic flux density arising from current I_1 and the integration is over S_2, the surface of coil 2 .

Using a magnetic vector potential $\boldsymbol{A}$ defined as,

$$\boldsymbol{B}_1 = \nabla \times \boldsymbol{A}_1, \tag{3.2}$$

and applying Stoke's theorem, we obtain

$$M_{12} = \frac{\oint_{C_2} \boldsymbol{A}_1 \cdot d\boldsymbol{l}_2}{I_1}, \tag{3.3}$$

$$\boldsymbol{A}_1 = \frac{\mu}{4\pi} \oint_{C_1} \frac{d\boldsymbol{i}_1}{R} = \frac{\mu I_1}{4\pi} \oint_{C_1} \frac{d\boldsymbol{l}_1}{R}, \tag{3.4}$$

where

$d\boldsymbol{i}_1$ is the current element in coil 1;

$d\boldsymbol{l}_1$ and $d\boldsymbol{l}_2$ are the differential lengths on the loops C_1 and C_2, respectively;

R is the distance between the differential lengths $d\boldsymbol{l}_1$ and $d\boldsymbol{l}_2$.

3.2.2 Inductance For Circular Coils

Mutual Inductance Between Two Circular Coils

Due to the difficulty of solving the surface integral of Equation (3.1), in the literature M_{12} between two circular coils is calculated in the case where the distance between the two coils d is much larger than the radius r_1 of the larger coil and the magnetic flux density $\boldsymbol{B}_1$ generated by coil 1 is considered constant across the area S_2 bounded by the coil 2. This assumption does not hold well for telemetry designs in which the two coils are near to each other compared with the dimension of the coils. However, with the use of the magnetic vector potential, the calculation of the mutual inductance is simplified to two contour integrals.

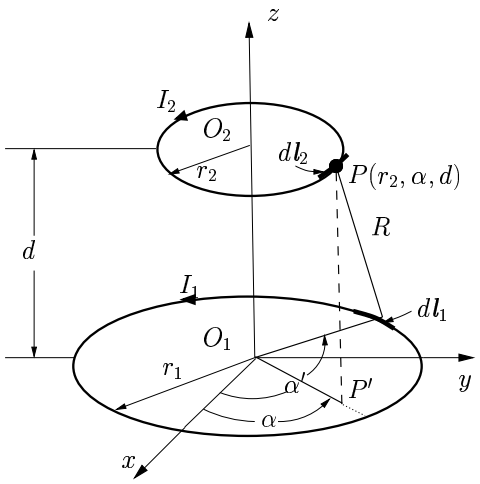

Figure 3.1: Mutual inductance calculation for two parallel circular loops.

As Figure 3.1 shown, two parallel circular coils are initially located a distance d apart on a common axis perpendicular to their planes. Current I_1 flows through coil 1. O_1 and O_2 are the origins in the two loops, and r_1 and r_2 are the radii of coil 1 and coil 2 respectively.

Considering the magnetic vector potential generated by a circular loop in spherical coordinates given by [17], in cylindrical coordinates, for a point $P(r_2, \alpha, z)$ on coil 2, the

magnetic vector potential $\boldsymbol{A}_1$ generated by coil 1 is

$$\boldsymbol{A}_1 = \boldsymbol{a}_\phi \frac{\mu_0 I_1 r_1}{4\pi} \int_0^{2\pi} \frac{\cos\theta \, d\theta}{\sqrt{(r_1^2 + r_2^2 + z^2 - 2r_1 r_2 \cos\theta}}, \tag{3.5}$$

where $\theta = \alpha - \alpha'$. Due to the symmetry, the magnetic potential only has the azimuthal component $A_{\phi 1}$.

With the substitution $\theta = \pi + 2\beta$, solving

$$A_{\phi 1} = \frac{\mu_0 I_1 r_1}{\pi} \int_0^{2\pi} \frac{(2\sin^2\beta - 1)\, d\beta}{\sqrt{(r_1 + r_2)^2 + z^2 - 4r_1 r_2 \sin^2\beta}}, \tag{3.6}$$

we obtain

$$\begin{aligned} A_{\phi 1} &= \frac{\mu_0 I_1 r_1}{\pi} \left[\left(\frac{1}{2r_1 r_2} - \frac{k^2}{4r_1 r_2} \right) K(k) - \frac{1}{2r_1 r_2} E(k) \right] \\ &= \frac{\mu_0 I_1}{2\pi r_2} \left[\left(1 - \frac{k^2}{2} \right) K(k) - E(k) \right] \end{aligned} \tag{3.7}$$

where $K(k)$ and $E(k)$ are elliptic integrals of the first and second kinds, respectively, defined as:

$$K(k) = \int_0^{\frac{\pi}{2}} \frac{d\beta}{\sqrt{1 - k^2 \sin^2\beta}} \tag{3.8}$$

$$E(k) = \int_0^{\frac{\pi}{2}} \sqrt{1 - k^2 \sin^2\beta}\, d\beta \tag{3.9}$$

where

$$k^2 = \frac{4r_1 r_2}{(r_1 + r_2)^2 + z^2} \tag{3.10}$$

Substituting Equation (3.7) into Equation (3.3), we obtain

$$\begin{aligned} M_{12} &= \frac{A_{\phi 1} \cdot 2\pi r_2}{I_1} \\ &= \mu_0 \sqrt{r_1 r_2} \left[\left(\frac{2}{k} - k \right) K(k) - \frac{2}{k} E(k) \right] \end{aligned} \tag{3.11}$$

with k is defined the same as in Equation (3.10).

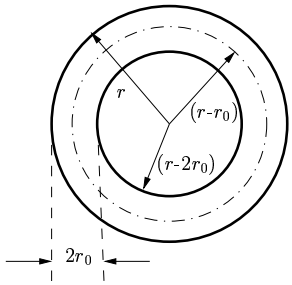

Figure 3.2: Self inductance calculation for a circle loop.

Self Inductance of a Circle Loop

We can use the mutual inductance derivation to calculate the external self inductance of a circular loop. As in Figure 3.2, if the wire radius r_0 is small compared with the loop radius r and skin effect is ignored, the external contribution of the self inductance is nearly the same as if currents were concentrated along the center of the wire. Therefore, we can approximate the external self inductance L_{ei} by using Equation (3.7) together with $z = 0$,

$$L_{ei} = \mu(2r - r_0)\left[\left(1 - \frac{k_2^2}{2}\right)K(k_2) - E(k_2)\right] \tag{3.12}$$

where $k_2^2 = \dfrac{4r(r - r_0)}{(2r - r_0)^2}$.

As for the internal self inductance of a circular loop, we approximate the magnetic field inside the loop to that which would be inside an imaginary infinite line conductor carrying the same current. With the internal self inductance per unit length for an infinite line conductor is $\mu/8\pi$, for the loop with a perimeter of $2\pi r$, the internal self inductance is

$$L_{ii} = \frac{\mu}{8\pi} \times 2\pi r = \frac{\mu r}{4} \tag{3.13}$$

Thus, the total self inductance is the sum of the external and internal self inductance

$$L_i = L_{ei} + L_{ii} = \mu(2r - r_0)\left[\left(1 - \frac{k_2^2}{2}\right)K(k_2) - E(k_2)\right] + \frac{\mu r}{4}. \tag{3.14}$$

Results

Table 3.1 shows the comparisons of the mutual inductances between the Elliptic integral analysis Section (3.2.2) and the empirical Terman's formula [8] The good agreement validated the calculation of the mutual inductance by the contour integrals of the magnetic vector potential.

Coil radius $r_1(mm)$	5	15	25	35	45	55	65
M_{12}(Elliptic integral)	0.0492	0.2528	0.3373	0.3321	0.3013	0.2682	0.2387
M_{12}(Terman's formula)	0.0491	0.2530	0.3374	0.3320	0.3016	0.2685	0.2389

Table 3.1: Comparative calculations of the mutual inductance between two circular loops with the distance $d = 2cm$ apart, and the secondary coil radius $r_2 = 3mm$.

3.2.3 Mutual Inductance Between Square Coils

The magnetic vector potential $\boldsymbol{A}$ can also be used to simplify the calculation of the mutual inductance between two square coils as shown in Figure 3.3. Because the vector

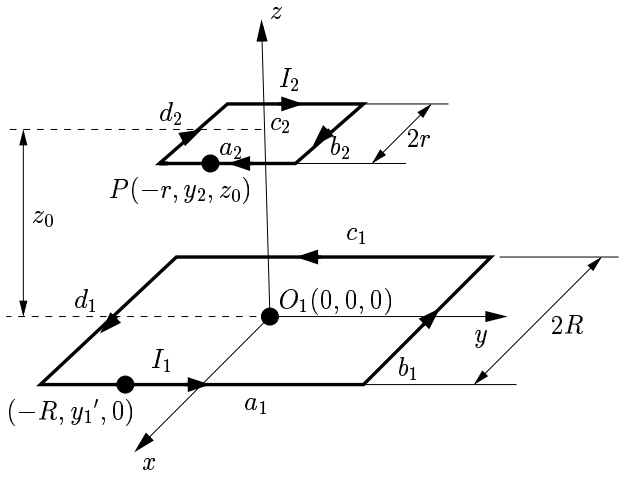

Figure 3.3: Mutual inductance calculation for two parallel square loops.

magnetic potential $\boldsymbol{A}_1$ is in the direction of the current element $d\boldsymbol{i}_1$ contributing to it by Equation (3.4), the contributions to $\boldsymbol{A}_1$ from the horizonal currents in the sides a_1

and c_1 of coil 1, are only horizontal. Therefore, these two sides contribute to the mutual inductance only through integration by Equation (3.3) over the two horizonal parts of coil 2, the sides a_2 and c_2. Similarly, the vertical currents in the sides b_1 and d_1 contribute to the mutual inductance only through integration by Equation (3.3) over the two vertical parts of coil 2, the sides b_2 and d_2.

Therefore, the mutual inductance between the two square coils is

$$\begin{aligned} M_{12} &= \frac{\oint_{C_2} \boldsymbol{A}_1 \cdot d\boldsymbol{l}_2}{I_1} \\ &= \frac{1}{I_1}\left(\int_{a_2+c_2} A_{a_1} dl_2 + \int_{a_2+c_2} A_{c_1} dl_2 + \int_{b_2+d_2} A_{b_1} dl_2 + \int_{b_2+d_2} A_{d_1} dl_2 \right). \end{aligned} \tag{3.15}$$

Because of the azimuthal symmetry of square loops, the contributions to the mutual inductance from each side of loop 1 are the same. Thus,

$$M_{12} = \frac{4}{I_1} \int_{a_2+c_2} A_{a_1} dl_2 \tag{3.16}$$

Now we calculate the magnetic potential contributed by side elements of the loop. From Equation (3.4), for a point $(-r, y_2, z_0)$ on side a_2, the magnetic vector potential A_{a_1} is

$$\begin{aligned} \boldsymbol{A}_{a_1 a_2} &= \boldsymbol{a}_y \frac{\mu I_1}{4\pi} \int_{-R}^{R} \frac{dy_1'}{\sqrt{(y_1'-y_2)^2 + (R-r)^2 + z_0^2}} \\ &= \boldsymbol{a}_y \frac{\mu I_1}{4\pi} \ln\left(y_1' - y_2 + \sqrt{(y_1'-y_2)^2 + (R-r)^2 + z_0^2} \right) \Big|_{-R}^{R} \\ &= \boldsymbol{a}_y \frac{\mu I_1}{4\pi} \ln \frac{R - y_2 + \sqrt{(R-y_2)^2 + (R-r)^2 + z_0^2}}{-R - y_2 + \sqrt{(R+y_2)^2 + (R-r)^2 + z_0^2}} \end{aligned} \tag{3.17}$$

Similarly, for a point (r, y_2, z_0) on side c_2, the magnetic potential A_{a_1} is

$$\boldsymbol{A}_{a_1 c_2} = \boldsymbol{a}_y \frac{\mu I_1}{4\pi} \ln \frac{R - y_2 + \sqrt{(R-y_2)^2 + (R+r)^2 + z_0^2}}{-R - y_2 + \sqrt{(R+y_2)^2 + (R+r)^2 + z_0^2}} \tag{3.18}$$

Moreover, since

$$\int_{a_2} \boldsymbol{A}_{a_1} \cdot d\boldsymbol{l}_2 = \int_{-r}^{r} A_{a_1 a_2} dy_2 \tag{3.19}$$

$$\int_{c_2} \boldsymbol{A}_{a_1} \cdot d\boldsymbol{l}_2 \;=\; -\int_{-r}^{r} A_{a_1 c_2} dy_2, \tag{3.20}$$

Equation (3.16) becomes

$$M_{12} = \frac{4}{I_1}\left(\int_{-r}^{r} A_{a_1 a_2} dy_2 - \int_{-r}^{r} A_{a_1 c_2} dy_2\right) \tag{3.21}$$

With

$$\int \ln(-u + \sqrt{u^2 + c})du = \ln(-u + \sqrt{u^2 + c}) \cdot u + \sqrt{u^2 + c} \tag{3.22}$$

we have

$$\begin{aligned} M_{12} \;=\; \frac{\mu}{\pi}\Big\{ & \ln\left[-(R+r) + \sqrt{2(R^2+r^2)+z_0^2}\,\right] \cdot (R+r) + \sqrt{2(R^2+r^2)+z_0^2} \\ & - \ln\left[-(R-r) + \sqrt{2(R-r)^2+z_0^2}\,\right] \cdot (R-r) + \sqrt{2(R-r)^2+z_0^2} \\ & + \ln\left[-(R+r) + \sqrt{2(R+r)^2+z_0^2}\,\right] \cdot (R+r) + \sqrt{2(R+r)^2+z_0^2} \\ & - \ln\left[-(R-r) + \sqrt{2(R^2+r^2)+z_0^2}\,\right] \cdot (R-r) + \sqrt{2(R^2+r^2)+z_0^2}\Big\} \end{aligned} \tag{3.23}$$

3.3 System Design of an Inductively Coupled Link

3.3.1 Survey of an Inductively Coupled Link Design

The design of a biomedical inductively coupled telemetry system is challenging because of the strict requirements such as small size, light weight, high efficiency, stable output and tissue energy absorption consideration. It is generally approached in two stages. First, the coupling coefficient is determined for various coil shapes and sizes, with specifications on the anticipated spacing and the accepted misalignments. Second, circuits must be designed to satisfy some requirements for good efficiency gain with sufficient bandwidth and low sensitivity to changes in k.

Throughout the design, a compromise has to be made between the magnitude of the coupling coefficient k and the position sensitivity of k. [2]-[4] have described the benefits in position tolerance from operating the link at, or near, critical coupling. For two coupled tuned circuits, at critical coupling, a maximum in the secondary circuit voltage occurs at

some value of coupling coefficient k_{crit} where the rate of changes in voltage with respect to changes in k is zero. It follows that operating coils at, or close to, $k = k_{crit}$ will achieve reasonable efficiency and good displacement tolerance simultaneously.

Moreover, in order to achieve the requirements of the system, during the choice of coils three main balances were [2]:

- For the transmitter primary coil diameter: higher working k against displacement tolerance;
- For the driver stage output resistance: lower k_{crit} against losses in the previous stage;
- For the receiver secondary coil loss resistance: lower k_{crit} against losses in the receiver.

In the literature, there exists considerable knowledge and practical examples on the design of inductive links [2]-[4]. In [3], stagger tuning of the coils has been used to desensitize the voltage transfer ratio without sacrificing efficiency. A geometric approach has been proposed by Galbraith *dt al.* [4] in which the coupling coefficient will remain fairly constant as long as the implanted secondary coil is within the perimeter of the external primary coil.

No matter which method is used in the design, there is no exact perfect group of parameters to optimize the efficiency of the power transfer and insensitivity of misalignment at the same time. An iterative trial-and-error procedure involving a number of possibilities is necessary to carry out to deal with the tradeoff between efficiency and misalignment tolerance.

3.3.2 Current Ratio of Primary and Secondary Coils

Because the sizes of the coils involved are small compared with the shortest wavelength present, coils can be treated as a quasi-static magnetic field problem. The principle configuration of transcutaneous inductively coupled coils is shown in Figure 3.4.

From Faraday's law of electromagnetic induction, the electromotive force induced in a stationary closed circuit is equal to the negative rate of increase of the magnetic flux

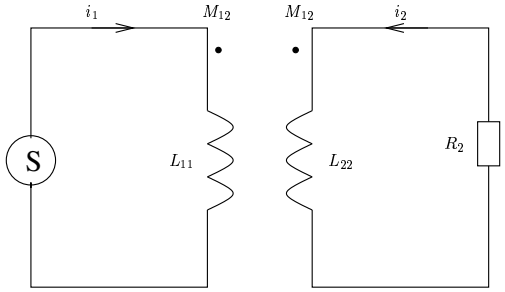

Figure 3.4: Principle configuration of the telemetry coil system.

linking the circuit. For the secondary coil 2, the total electromotive force is zero, and it consists of two parts $R_2 i_2$ and $(d\Psi_2/dt)$ where R_2 is the resistance of the secondary coil 2 and Ψ_2 is the total magnetic flux with

$$\Psi_2 = M_{12} i_1 + L_{22} i_2 \tag{3.24}$$

where M_{12} is the mutual inductance between the primary and secondary coils, L_{22} is the self inductance of the secondary coil.

To determine the current i_2 in the secondary coil, we apply the above equations and obtain:

$$R_2 i_2 + \frac{d\Psi_2}{dt} = R_2 i_2 + M_{12}\frac{di_1}{dt} + L_{22}\frac{di_2}{dt} = 0 \tag{3.25}$$

With the initial condition $i_2(t = 0) = 0$ and the current in the primary coil $i_1(t) = I_0 \sin(\omega t)$, the solution to this linear differential equation is

$$\begin{aligned} i_2(t) &= e^{-\frac{R_2}{L_{22}}t}\left[-\int \frac{M_{12}}{L_{22}}\,\omega I_0 \cos(\omega t)\, e^{\frac{R_2}{L_{22}}t}\, dt + C\right] \\ &= Ce^{-\frac{R_2}{L_{22}}t} - \frac{\frac{M_{12}}{L_{22}}\,\omega I_0\left[\frac{R_2}{L_{22}}\cos(\omega t) + \omega \sin(\omega t)\right]}{\omega^2 + (\frac{R_2}{L_{22}})^2} \\ &= Ce^{-\frac{R_2}{L_{22}}t} - \frac{\omega M_{12} I_0\left[R_2 \cos(\omega t) + \omega L_{22}\sin(\omega t)\right]}{\omega^2 L_{22}^2 + R_2^2} \end{aligned} \tag{3.26}$$

The unknown constant C is decided by initial conditions. For $R_2 = 0$, the above solution becomes simply

$$i_2(t) = -\frac{M_{12}}{L_{22}} I_0 \sin(\omega t) \tag{3.27}$$

Thus, the magnitude ratio of the currents in the primary and secondary coils is

$$\left|\frac{i_2(t)}{i_1(t)}\right| = \left|\frac{-\frac{M_{12}}{L_{22}} I_0 \sin(\omega t)}{I_0 \sin(\omega t)}\right| = \left|\frac{M_{12}}{L_{22}}\right| \tag{3.28}$$

The results by this quasi-static analysis have been compared with other computational electromagnetic methods as shown in Figure 4.3.

3.3.3 Frequency

The choice of the carrier frequency is governed by two main considerations: tissue absorption and the compactness of the implanted system. Since tissue absorption increases with the frequency [25], the upper limit of the frequency is imposed by tissue absorption. Moreover, skin effect in high frequencies results in conductor losses of the coupling coils. The lower limit of the frequency mainly depends on the signal bandwidth. Sometimes the medium waveband radio interference also has to be taken into account.

Chapter 4

The Thin-Strut FDTD formalism

4.1 Introduction

In FDTD, wires are usually modelled as perfect electric conductors by forcing all tangential electric field components on their surfaces to zero. For wires with very small cross-sections, a very high resolution grid is necessary in order to accurately model the wires. But FDTD with such a high resolution grid is prohibitively computational expensive.

In order to model these small but important structural features with possible run time and few nodes, several modified thin-wire subcell FDTD formalisms have been proposed in the literature, such as the thin-strut FDTD formalism [14], the Faraday's law contour-path model [13], the transmission line modelling technique (TLM) [27], the Finite Volumes and Finite Elements methods with unstructured mesh time-domain solvers [28]-[29], and hybrid techniques combining the MOM in time-domain and FDTD [30].

The thin-strut FDTD formalism by Holland *et al.* captured the effects of a thin wire present in the discretized three-dimensional space by introducing an "in-cell inductance" model of the wire. The wire was separated from the three-dimensional volume, and partial differential equations governing currents and charge densities on the wire were developed. Then the simultaneous, coupled equations for currents and charge densities were solved concurrently with the FDTD time stepping.

Several extensions to the basic wire models for volumetric solvers also have been de-

veloped. A multiwire formalism to include bundled wires [26] is presented by Bérenger based on the thin-strut FDTD formalism [14]. It is very useful to treat several wires running close together. In [31], Douglas *et al.* improved the basic assumption in [13] that the normal electric fields and the tangential magnetic fields are both inversely proportional to wire radius r, along the wire.

As we are mainly concerned with biomedical telemetry system designs, the specifications in the sizes of the coils and the frequency of use make the subcell FDTD model of Holland *et al.* [14] a very attractive tool to numerically analyze the electromagnetic fields around coils. With the extended use of Holland's method to model the coupling between the primary and secondary coils, the ratio of the currents in the two coils has been calculated for different configurations of the coils.

The outline of the rest of this chapter is as follows: In the next section the coupling field-wire system equations are established. Then an approximated in-cell inductance is introduced. Since the CFL stability condition of the conventional FDTD method is not sufficient to stabilize the new field-wire system, we discuss the stability and the convergence of the new system, from the unconditionally stable semi-discrete field-wire system to conditionally stable fully-discrete system. A new stability criterion for selecting the time step is introduced and is in agreement with numerical simulations. The results of our extension of the thin-strut FDTD formalism were compared with those obtained by the conventional FDTD method, the quasi-static analysis in Section 3.2.3, and the NEC code (MOM).

4.2 Coupling Between Field and Wire

4.2.1 Governing Equations

Following [14], we derive a suitable wire equation to separate the wire from the three dimensional volume. We begin with the study of an infinite long cylinder of radius a running in the z-direction in free space, see Figure 4.1.

With $\boldsymbol{M} = 0$, and two constitutive equations: $\boldsymbol{B} = \mu_0 \boldsymbol{H}$ and $\boldsymbol{D} = \epsilon_0 \boldsymbol{E}$, Maxwell's

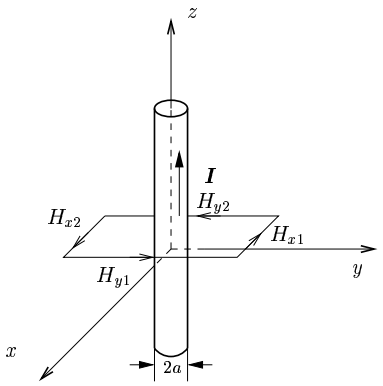

Figure 4.1: An infinite thin wire with the current I running in the z direction.

equations (2.1) and (2.2) become

$$\epsilon_0 \frac{\partial \boldsymbol{E}}{\partial t} = \nabla \times \boldsymbol{H} - \boldsymbol{J} \tag{4.1}$$

$$\mu_0 \frac{\partial \boldsymbol{H}}{\partial t} = -\nabla \times \boldsymbol{E} \tag{4.2}$$

Together with the periodic boundary condition for the H_z component, taking the r component of Ampere's law equation (4.1) in cylindrical coordinates gives

$$\frac{1}{r}\frac{\partial H_z}{\partial \theta} - \frac{\partial H_\theta}{\partial z} = \epsilon \frac{\partial E_r}{\partial t} \quad \text{with } H_z(r,0) = H_z(r,2\pi) \tag{4.3}$$

Integration of Equation (4.3) from $\theta = 0$ to 2π gives ,

$$\begin{aligned} \epsilon \frac{\partial}{\partial t}\int_0^{2\pi} E_r \, d\theta &= \frac{1}{r}\frac{\partial}{\partial \theta}\int_0^{2\pi} H_z \, d\theta - \frac{\partial}{\partial z}\int_0^{2\pi} H_\theta \, d\theta \\ &= -\frac{\partial}{\partial z}\int_0^{2\pi} H_\theta \, d\theta \end{aligned} \tag{4.4}$$

Moreover, with the boundary condition on the wire surface, the θ component of Faraday's law equation (4.2) in cylindrical coordinates becomes

$$\frac{\partial E_z}{\partial r} - \frac{\partial E_r}{\partial z} = \mu \frac{\partial H_\theta}{\partial t} \quad \text{with } E_z(r \le a) = 0 \tag{4.5}$$

Integration of Equation (4.5) from $r = a$ to R gives,

$$\begin{aligned} \mu \frac{\partial}{\partial t}\int_a^R H_\theta \, dr &= \frac{\partial}{\partial r}\int_a^R E_z \, dr - \frac{\partial}{\partial z}\int_a^R E_r \, dr \\ &= \langle E_z(R) \rangle - E_z(a) - \frac{\partial}{\partial z}\int_a^R E_r \, dr \end{aligned} \tag{4.6}$$

With $E_z(a) = 0$, we have

$$\langle E_z(R)\rangle = \mu\frac{\partial}{\partial t}\int_a^R H_\theta\, dr + \frac{\partial}{\partial z}\int_a^R E_r\, dr \tag{4.7}$$

where $\langle E_z(R)\rangle$ is the average value of the electric fields over the equivalent area if the wire is not placed on the edge of the FDTD mesh.

As mentioned in Section 3.1, thin wires in the three-dimensional field volume can be treated as a quasi-static field problem as long as the sizes of the wires involved are small compared with the shortest wavelength present. That is to say, if the interactions between the wire and the surrounding fields have a much smaller time variation than the space variation, we can use Biot-Savart's law and Coulomb's law to explain the relation between the field and the wire. Biot-Savart's law for a direct current I in an infinite long wire is,

$$H_\theta(r) = \frac{I}{2\pi r} \tag{4.8}$$

and Coulomb's law for the charge per unit length Q on an infinite long wire is

$$E_r(r) = \frac{Q}{2\pi r\epsilon} \tag{4.9}$$

Substituting Equation (4.8) and (4.9) into Equation (4.7), we have

$$\begin{aligned}\langle E_z(R)\rangle &= \frac{\mu}{2\pi}\frac{\partial I}{\partial t}\int_a^R \frac{1}{r}\, dr + \frac{1}{2\pi\epsilon}\frac{\partial Q}{\partial z}\int_a^R \frac{1}{r}\, dr \\ &= \frac{\mu}{2\pi}\ln(\frac{R}{a})\frac{\partial I}{\partial t} + \frac{1}{2\pi\epsilon}\ln(\frac{R}{a})\frac{\partial Q}{\partial z}\end{aligned} \tag{4.10}$$

Introducing an in-cell inductance per unit length of the wire $L(R)$ in $Henry/meter$,

$$L(R) = \frac{\mu}{2\pi}\ln(\frac{R}{a}), \tag{4.11}$$

Equation (4.10) becomes

$$\langle E_z(R)\rangle = L(R)\left[\frac{\partial I}{\partial t} + \frac{1}{\mu\epsilon}\frac{\partial Q}{\partial z}\right] \qquad \text{for } R > a \Rightarrow \tag{4.12}$$

$$\frac{\partial I}{\partial t} + \frac{1}{\mu\epsilon}\frac{\partial Q}{\partial z} = \frac{\langle E_z(R)\rangle}{L(R)} \tag{4.13}$$

From the equation of continuity (2.5), we have

$$\frac{\partial I}{\partial z} = -\frac{\partial Q}{\partial t} \tag{4.14}$$

Now we have two sets of equations as system equations:

$$\begin{aligned} \epsilon \frac{\partial \boldsymbol{E}}{\partial t} &= \nabla \times \boldsymbol{H} - \boldsymbol{J} & \qquad \frac{\partial I}{\partial t} + \frac{1}{\mu\epsilon}\frac{\partial Q}{\partial z} &= \frac{\langle E_z(R)\rangle}{L(R)} \\ \mu \frac{\partial \boldsymbol{H}}{\partial t} &= -\nabla \times \boldsymbol{E} & \qquad \frac{\partial I}{\partial z} &= -\frac{\partial Q}{\partial t} \end{aligned} \tag{4.15}$$

The coupling between the field equations and the wire equations is through the source terms $\boldsymbol{J}$ and $\boldsymbol{E}$. After using the central finite difference approximations up to second order accuracy for both temporal and spatial derivatives in the equations above and approximating the current density $\boldsymbol{J}$ by distributing the current from the wire to the surrounding field components, $J = I/S_{cross}$, where S_{cross} is the area of the occupied cell, we obtain,

$$I_z|_k^{n+\frac{1}{2}} = I_z|_k^{n-\frac{1}{2}} + \frac{\Delta t}{L}\left(\langle E_z(R)\rangle^n - L\,\frac{Q_z|_{k+\frac{1}{2}}^n - Q_z|_{k-\frac{1}{2}}^n}{\mu\epsilon\Delta z}\right) \tag{4.16}$$

$$Q_z|_{k-\frac{1}{2}}^{n+1} = Q_z|_{k-\frac{1}{2}}^n - \Delta t\left(\frac{I_z|_k^{n+\frac{1}{2}} - I_z|_{k-1}^{n+\frac{1}{2}}}{\Delta z}\right) \tag{4.17}$$

together with the updating equations for fields in Section 2.2.3.

Note that, for the wire with the current I_z running along z direction, I_z, J_z and E_z are collocated, while Q_z and H_z are collocated. Moreover, if I_z and $\boldsymbol{H}$ are updated at the same time-step $t = (n+\frac{1}{2})\Delta t$; Q_z and $\boldsymbol{E}$ are updated at a half time-step later $t = (n+1)\Delta t$ where n is an integer. The field and wire quantities are solved in a "leap-frog" fashion with a half time step between them.

4.2.2 Approximation of the In-Cell Inductance

In Equation (4.13), the introduced in-cell inductance $L(R)$ is a function of R. It gives Equation (4.13) a variable coefficient. In order to simplify the above equation into a constant coefficient PDE, we need to make some approximations to determine $L(R)$. This depends on how to choose the radius R.

If considering a discrete field component also represents the field averaged over the surface, we have $R = h/2$, assuming the resolutions over the three directions are the same, $\Delta x = \Delta y = \Delta z = h$. Substituting this into Equation (4.11), we have

$$L_{h/2} = \frac{\mu}{2\pi} \ln(\frac{h}{2a}) \tag{4.18}$$

An alternative is to take an average of Equation (4.13) over a circle with the same area of the wire-occupied FDTD cell. Then the radius of the equivalent circle is

$$R = \sqrt{\frac{4}{\pi}}\, h \tag{4.19}$$

Substituting this into Equation (4.11), we obtain

$$\begin{aligned} L_{equiS} &= \frac{\int_0^{2\pi}\int_0^R r\frac{\mu}{2\pi}\ln(\frac{r}{a})\, dr\, d\theta}{\int_0^{2\pi}\int_0^R r\, dr\, d\theta} \\ &= \frac{\mu}{2\pi}\left[\ln(\frac{R}{a}) - \frac{1}{2} + \frac{a^2}{2R^2}\right] \\ &= \frac{\mu}{2\pi}\left[\ln(\frac{2h}{\sqrt{\pi}a}) - \frac{1}{2} + \frac{a^2\pi}{8h^2}\right] \end{aligned} \tag{4.20}$$

Figure 4.2 shows that the in-cell inductance L is inversely proportional to the normalized wire radius a/h. And there is no significant difference between the results from the above two kinds of approximations of the in-cell inductance.

$$\begin{aligned} &\frac{a}{h} \geq \frac{1}{2}\,, \qquad L_{h/2} \leq 0; \\ &\frac{a}{h} \geq 0.9725,\ L_{equiS} \leq 0. \end{aligned}$$

Note that when the diameter of the wire equals to the cell size, the wire occupies the whole cell. If we still insist on using the thin-strut formalism, a singular problem will present, as discussed in Section 4.3.1. In that case, the simplest and most accurate method is to model the wire as the conventional FDTD does.

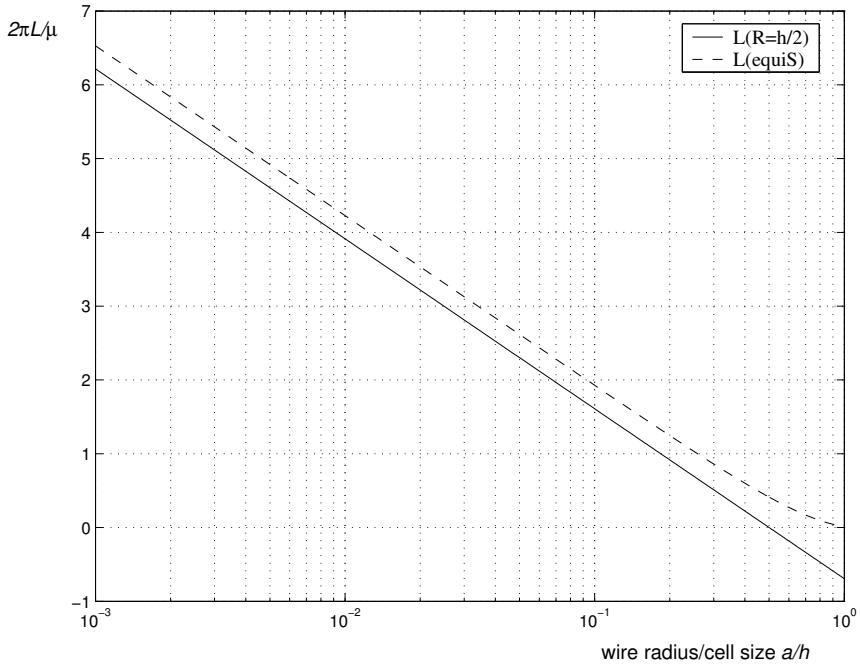

Figure 4.2: Comparative calculations of normalized in-cell inductance per unit length ($2\pi L/\mu$) versus normalized wire radius (a/h)

4.3 Stability and Convergence Analyses

4.3.1 Unconditionally Stable Semi-Discrete Field-Wire System

It is well known that both Maxwell's equations and the wire equations (4.15) are well-posed. But the coupled system of these two are not guaranteed to be well-posed too. If one attempts to apply finite difference methods blindly, it is very easy to create one that is unstable. Therefore, it is essential to study the stability of the coupled system. We start the stability analysis from the equivalent semi-discrete field-wire system since the stability of the semi-discrete field-wire system is a necessary stability condition for the fully-discrete one.

Considering the general case where $\boldsymbol{I}$ and $\boldsymbol{Q}$ may run at any direction, we write the field-wire system in matrix form:

$$\frac{\partial}{\partial t}\begin{pmatrix} \boldsymbol{E}(t) \\ \boldsymbol{H}(t) \\ \boldsymbol{I}(t) \\ \boldsymbol{Q}(t) \end{pmatrix} = \begin{pmatrix} 0 & \mathcal{S} & \mathcal{U} & 0 \\ \mathcal{T} & 0 & 0 & 0 \\ \mathcal{V} & 0 & 0 & \mathcal{M} \\ 0 & 0 & \mathcal{N} & 0 \end{pmatrix} \begin{pmatrix} \boldsymbol{E}(t) \\ \boldsymbol{H}(t) \\ \boldsymbol{I}(t) \\ \boldsymbol{Q}(t) \end{pmatrix} \tag{4.21}$$

where the operators $\mathcal{S}$, $\mathcal{T}$, $\mathcal{U}$ and $\mathcal{V}$ take care of the spatial discretization of the field equations, while the operators $\mathcal{M}$ and $\mathcal{N}$ take care of those of the wire equations. For example,

$$\mathcal{S} = \frac{1}{\epsilon}(\nabla\times\,) \qquad \text{and} \qquad \mathcal{T} = -\frac{1}{\mu}(\nabla\times\,). \tag{4.22}$$

Some important symmetries of Equation (4.21) can be made explicit by introducing the scaling of the following variables:

$$\begin{aligned} \boldsymbol{h}(t) &= \sqrt{\mu}\,\boldsymbol{H}(t) & \boldsymbol{i}(t) &= \sqrt{\mu}\,\sqrt{L_n}\,\boldsymbol{I}(t) \\ \boldsymbol{e}(t) &= \sqrt{\epsilon}\boldsymbol{E}(t) & \boldsymbol{q}(t) &= \frac{\sqrt{\epsilon}}{\sqrt{L_n}}\,\boldsymbol{Q}(t) \end{aligned} \tag{4.23}$$

with $L_n = L/\mu$.

Substituting Equation (4.23) into Equation (4.21), we have

$$\frac{\partial}{\partial t}\begin{pmatrix} \boldsymbol{e}(t) \\ \boldsymbol{h}(t) \\ \boldsymbol{i}(t) \\ \boldsymbol{q}(t) \end{pmatrix} = \begin{pmatrix} 0 & \hat{\mathcal{S}} & \hat{\mathcal{U}} & 0 \\ \hat{\mathcal{T}} & 0 & 0 & 0 \\ \hat{\mathcal{V}} & 0 & 0 & \hat{\mathcal{M}} \\ 0 & 0 & \hat{\mathcal{N}} & 0 \end{pmatrix} \begin{pmatrix} \boldsymbol{e}(t) \\ \boldsymbol{h}(t) \\ \boldsymbol{i}(t) \\ \boldsymbol{q}(t) \end{pmatrix} = P \begin{pmatrix} \boldsymbol{e}(t) \\ \boldsymbol{h}(t) \\ \boldsymbol{i}(t) \\ \boldsymbol{q}(t) \end{pmatrix} = P\Psi(\mathrm{t}) \tag{4.24}$$

where P is skew symmetric, i.e., $P^T = -P$, with respect to the inner product

$$\langle \Psi | \Psi' \rangle \equiv \int_V \Psi^T \cdot \Psi'\, dr, \tag{4.25}$$

where V denotes the volume of the enclosing box. That is to say,

$$\begin{aligned} \hat{\mathcal{S}}^T &= -\hat{\mathcal{T}} \\ \hat{\mathcal{U}}^T &= -\hat{\mathcal{V}} \\ \hat{\mathcal{M}}^T &= -\hat{\mathcal{N}} \end{aligned} \tag{4.26}$$

The formal solution of Equation (4.24) is

$$\Psi(t) = e^{t\,P}\Psi(0) \tag{4.27}$$

Defining the total electromagnetic energy of the field-wire system as

$$\mathcal{W}\left(\mathrm{t}\right) \equiv \frac{1}{2}\left(\boldsymbol{e}^{\mathrm{T}}\,\boldsymbol{e} + \boldsymbol{h}^{\mathrm{T}}\,\boldsymbol{h} + \boldsymbol{i}^{\mathrm{T}}\,\boldsymbol{i} + \boldsymbol{q}^{\mathrm{T}}\,\boldsymbol{q}\right) \tag{4.28}$$

we have

$$\frac{\partial \mathcal{W}}{\partial t} = \Psi^T P \Psi. \tag{4.29}$$

Since $\Psi^T P \Psi$ is 1×1 matrix, $(\Psi^T P \Psi)^T = \Psi^T P \Psi$; meanwhile, with the characteristic of the skew symmetric matrix P, we have

$$(\Psi^T P \Psi)^T = \Psi^T P \Psi = -\Psi^T P \Psi \tag{4.30}$$

Thus, to satisfy $\Psi^T P \Psi = -\Psi^T P \Psi$, $\Psi^T P \Psi$ has to be zero. Therefore,

$$\frac{\partial \mathcal{W}}{\partial t} = 0. \tag{4.31}$$

This means that the total electromagnetic energy does not change with time and is preserved.

A necessary and sufficient condition for an algorithm to be unconditionally stable is that the length of $\Psi(t)$ should be bounded, for arbitrary initial condition $\Psi(t = 0)$ and for any time t [16]. By construction of

$$\|\Psi(t)\|^2 = \langle \Psi(t) | \Psi(t) \rangle = \int_V \mathcal{W}(\mathrm{t})\mathrm{d}\boldsymbol{r}, \tag{4.32}$$

we notice that the length of $\|\Psi(t)\|$ will not change with time and is always bounded. Thus, the semi-discrete field-wire system is unconditionally stable.

4.3.2 Conditionally Stable Fully-Discrete Field-Wire System

Based on Ampere's law Equation (2.2) in the integral form

$$\oint_c \boldsymbol{H} \cdot d\boldsymbol{l} = I, \tag{4.33}$$

for a rectangular FDTD mesh, with space increments $\Delta x \neq \Delta y$ and the current I is flowing in the z direction, see Figure 4.1, we have

$$
\begin{aligned}
H_{y1} &= -H_{y2} = \frac{I}{\pi\,\Delta x} \\
H_{x1} &= -H_{x2} = -\frac{I}{\pi\,\Delta y}
\end{aligned}
\tag{4.34}
$$

Moreover, the electric current density J is approximated by $J = I/S_{cross}$, independent of the wire radius. After substituting Equation (4.34) into Equation (4.15), together with the relation equation $c^2 = 1/(\mu_0\epsilon_0)$ for free space where c is the speed of light in free space, and applying the central difference scheme to approximate the partial derivatives in both time and space, we obtain

$$
\frac{\partial^2 I}{\partial t^2} = c^2 \frac{\partial^2 I}{\partial z^2} - AI \tag{4.35}
$$

where

$$
A = \frac{\mu c^2}{L}\left[\frac{1}{S_{cross}} - \frac{2}{\pi}\left(\frac{1}{\Delta x^2} + \frac{1}{\Delta y^2}\right)\right] \tag{4.36}
$$

If $\Delta x = \Delta y = h$,

$$
A = \frac{\mu c^2}{Lh^2}\left(\frac{h^2}{S_{cross}} - \frac{4}{\pi}\right). \tag{4.37}
$$

Von Neumann Stability Analysis

Based on the Fourier analysis, the Von Neumann stability analysis [32] demonstrates a necessary condition for stability. It serves as a check on whether or not the finite difference method can ever be stable.

Approximating the partial derivatives in Equation (4.35) by the central difference scheme gives

$$
\frac{I_k^{n+1} - 2I_k^n + I_k^{n-1}}{(\Delta t)^2} = c^2 \frac{I_{k+1}^n - 2I_k^n + I_{k-1}^n}{h^2} - AI_k^n \tag{4.38}
$$

with $I_k^n = I(n\Delta t, kh) = I(n,k)$.

While the Von Neumann analysis is derived from a Fourier series representation of a finite difference problem, it can be used directly with its generalized Fourier components. Each discrete value in the difference equation (4.38) is replaced with its generalized Fourier component,

$$\begin{aligned} I_k^n &= g(\xi,\Delta t,h)^n e^{i\xi h\cdot k} \\ I_{k+1}^n &= g(\xi,\Delta t,h)^n e^{i\xi h\cdot (k+1)} \\ I_{k-1}^n &= g(\xi,\Delta t,h)^n e^{i\xi h\cdot (k-1)} \\ I_k^{n+1} &= g(\xi,\Delta t,h)^{n+1} e^{i\xi h\cdot k} \end{aligned} \tag{4.39}$$

where $e^{i\xi} = cos(\xi) + i \cdot sin(\xi)$, $i = \sqrt{-1}$, $0 \le \xi h < 2\pi$, $g(\xi,\Delta t,h)$ is the growth factor. Specially, if $g(\xi,\Delta t,h)$ is independent of Δt and h, $g(\xi,\Delta t,h) = g(\xi)$.

If $|g(\xi)| \le 1$, then $|I^{n+1}| \le |I^n|$, and thus the stability of the thin-strut finite difference formalism is ensured.

Replacing Equation (4.38) with its Von Neumann's form gives,

$$\frac{|g(\xi)| - 2 + |g(\xi)|^{-1}}{(\Delta t)^2} = c^2 \frac{e^{i\xi h} - 2 + e^{-i\xi h}}{h^2} - A$$

$$|g(\xi)| - 2 + |g(\xi)|^{-1} = \left(c^2 \frac{e^{i\xi h} - 2 + e^{-i\xi h}}{h^2} - A \right) \cdot (\Delta t)^2 = B$$

After arrangement, we obtain

$$|g(\xi)|^2 - (2+B)|g(\xi)| + 1 = 0 \tag{4.40}$$

$$|g(\xi)| = \frac{2 + B \pm \sqrt{(2+B)^2 - 4}}{2} = \frac{2+B}{2} \pm \sqrt{\left(\frac{2+B}{2}\right)^2 - 1} \tag{4.41}$$

Let $a = \dfrac{2+B}{2}$, then $|g(\xi)| = a \pm \sqrt{a^2 - 1}$. If $a^2 - 1 \le 0$, $g(\xi) = a \pm i\sqrt{1 - a^2}$, then $|g(\xi)| = \sqrt{a^2 + (1 - a^2)} = 1$ always and the stability is assured.

So we need $|a| = \left| \dfrac{2+B}{2} \right| \le 1$, i.e.,

$$-4 \le B = \left(c^2 \frac{e^{i\xi h} - 2 + e^{-i\xi h}}{h^2} - A \right) \cdot (\Delta t)^2 = \left(c^2 \, \frac{2\cos(\xi h) - 2}{h^2} - A \right) \cdot (\Delta t)^2 \le 0 \tag{4.42}$$

The useful inequality is the left hand side of Equation (4.42), see [16], so we have

$$B_{min} = (c^2 \, \frac{-4}{h^2} - A) \cdot (\Delta t)^2 \ge -4. \tag{4.43}$$

After substituting Equation (4.37) into A, the final requirement for stability is

$$\Delta t \leq \frac{1}{\sqrt{\frac{A}{4}+\frac{c^2}{h^2}}} = \frac{h}{c}\cdot\frac{1}{\sqrt{1+\frac{\mu_0}{\pi L}\left(\frac{1}{4S_{cross}}-1\right)}} = \Delta t_2 \tag{4.44}$$

Compared with the CFL stability limit condition Equation (2.25)

$$\Delta t \leq \frac{h}{c}\cdot\frac{1}{\sqrt{3}} = \Delta t_1, \tag{4.45}$$

to ensure the system stable, the time step has to satisfy the conditions below:

$$\begin{aligned} &\Delta t \leq \Delta t_1, \quad \text{for } \Delta t_1 \leq \Delta t_2; \\ &\Delta t \leq \Delta t_2, \quad \text{for } \Delta t_1 \geq \Delta t_2. \end{aligned} \tag{4.46}$$

The inequality equation above tells us how to set the parameters in the thin-strut FDTD formalism to ensure the stability. Since the in-cell inductance L increases with the decrease of normalized wire radius a/h, see Figure 4.2, resulting in a larger Δt_2 by the inequality (4.44), the wire radius must be small enough so that $\Delta t_1 \leq \Delta t_2$ is satisfied, which in turn ensures $\Delta t \leq \Delta t_1$. Therefore, to ensure the stability of the new system, if the time step of the new system remains the same as that of the conventional FDTD simulation, the wire radius need to be set small enough; otherwise, the time step has to be decreased according to Equation (4.46).

Along with the criterion to avoid grid dispersion, this stability condition allows us to choose proper space and time sampling for the thin-strut finite difference formalism.

4.3.3 Consistency

We use the central difference scheme to approximate Equation (4.35) with Equation (4.38). The corresponding local truncation error is

$$\begin{aligned} T(t_n, z_k) &= \frac{I_k^{n+1}-2I_k^n+I_k^{n-1}}{(\Delta t)^2} - \left[c^2\frac{I_{k+1}^n-2I_k^n+I_{k-1}^n}{h^2} - AI_k^n\right] \\ &= \frac{\partial^2 I_k^n}{(\partial t)^2} + O\left[(\Delta t)^2\right] - \left[c^2\frac{\partial^2 I_k^n}{\partial x^2} + O(h^2) - AI_k^n\right] \\ &= O\left[(\Delta t)^2 + h^2\right] \end{aligned} \tag{4.47}$$

From Equation (4.47), as $\Delta t \to 0, h \to 0, T(t_n, z_k) \to 0$. So the discretization is second order accurate in both time and space.

Without taking the roundoff error into account, the global error is the total error between the computed solution and the actual solution. Because the algorithm is stable, the errors from each time step can be added together. So the global error is also $O\left[(\Delta t)^2 + h^2\right]$. That means that the thin-strut formalism is consistent and second order accurate in time and space. Because a consistent and stable finite difference scheme is convergent [16], the thin-strut FDTD formalism is convergent.

4.4 Results

The thin-strut FDTD formalism has been extended to analyze the current ratio of the currents in the external and implanted coils. Simulations have been carried out with variations in the excitation source, the dimension of the primary external coil, the distance between two coils, and the frequency of sinusoidal excitation. We divide our simulations into two categories according to the excitation source: sinusoidal sources and Gaussian sources. For reference, calculations of the NEC code [6] is used.

As for circular loops, we have to treat the arbitrarily oriented wires by staircasing. Because errors introduced by the staircasing can be several tens of percent, it will increase the difficulty to judge the effectiveness and the accuracy of the thin-strut FDTD formalism. Therefore, we dealt with square loops. The structure shown in Figure 3.3 was analyzed: two parallel square coils were located a distance z_0 apart on a common axis perpendicular to their located planes, with an excitation current in the primary external coil 1 and a coupling current in the secondary internal coil 2. The following parameters were used: half length of the internal coil r=3mm, half length of the external coil R ranged from 5mm to 40mm, the distance z_0 ranged from 10mm to 35mm. The computational space was terminated with a 15 cell thick PML layer which is 10 cells away from the sides of the external coil. All the sources were excited as a current source, i. e., by updating the corresponding H fields around the wire according to the specific source function.

If R=25mm, z_0=20mm, the meshes used in these computations were: for the conven-

tional FDTD method, dz=1mm and dx=dy=0.5mm, the problem space was 150×150×80 cells with the time step of 0.83ps; in comparison, for the thin-strut FDTD formalism, dx=dy=dz=1mm, the problem space was 100 × 100 × 80 cells, the time step was Δt= $\frac{h}{2c_0}$=$\frac{0.001m}{2\times3\times10^8 m/s}$ ≈ 1.67ps, and the wire radius a=0.05mm or a=0.01mm which satisfied the stability inequality equations (4.46).

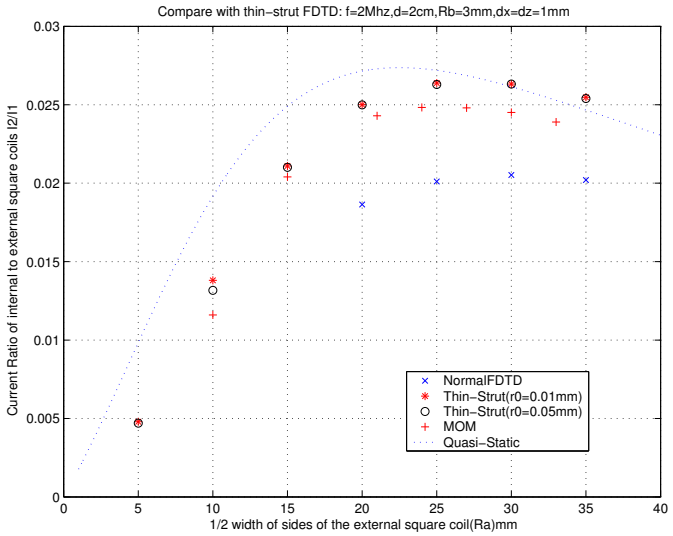

Figure 4.3: Current ratio (I_2/I_1) versus the half length of the external coil.

4.4.1 Sinusoidal Source

For a simulation with a 2MHz sinusoidal wave, a quarter cycle of a 2MHz wave is 15000 time steps. The general peak detection method or a Fourier Transform method requires the simulation should be run for a full cycle past convergence. That involves a large amount of computer time and memory, especially for low frequencies and high resolutions. In order to save computer time, the amplitude of the sinusoidal coupling current was calculated by the two-equations two-unknowns method in Section 2.2.5 which has been proved to be effective for several applications in [22]-[23]. The coupling currents were sampled at two time steps in the first quarter of the whole wave period.

Figure 4.3 provides a comparison with the conventional FDTD method, the thin-strut FDTD formalism with two different wire radii, the quasi-static analysis in Section 3.2.3,

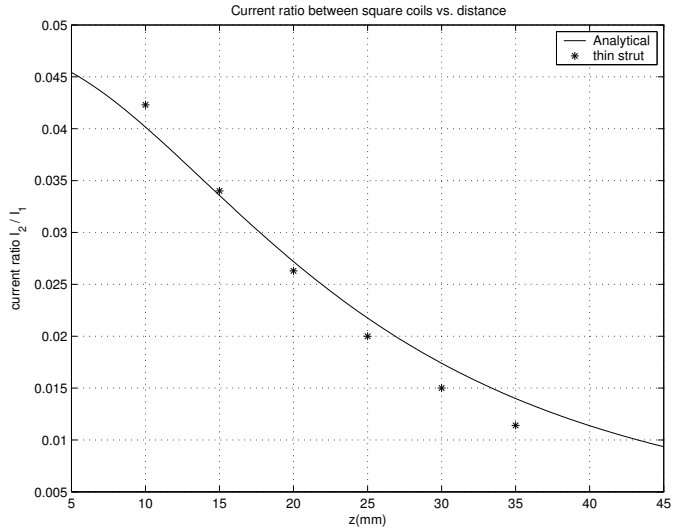

Figure 4.4: Current ratio (I_2/I_1) versus the distance between the external and internal coils.

and the NEC code (MOM).

Compared with the conventional FDTD method, both results from the thin-strut FDTD formalism with different wire radii are much more agreeable with those obtained from the NEC code and from the quasi-static analysis.

Figure 4.4 compares the results of current ratio from the thin-strut FDTD formalism and the quasi-static analysis as a function of the distance between the internal and external coils. Results are in good agreement.

4.4.2 Gaussian Source

Gaussian excitation current $I_1(t)$ in the time-domain is shown as Figure 4.5. The corresponding frequency-domain one was obtained by FFT, shown as Figure 4.6. Note that Gaussian pulse current source considered here satisfies

$$I_1 = \exp\left\{-\frac{1}{2}\,(\frac{T-t_0}{\sigma})^2\right\}. \tag{4.48}$$

where $t_0 = 30000$, $\sigma = 3500$ or 7000, T is the time step. The difference in t_0 have no effect on the corresponding frequency components in the frequency-domain. Only changes in σ will affect the wave shape in the frequency-domain. Because our frequency of interest

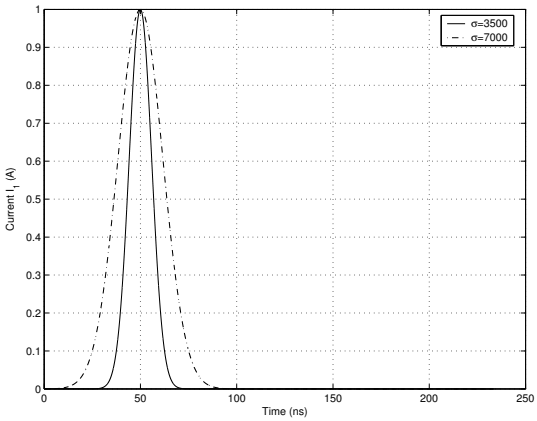

Figure 4.5: Comparison in the time-domain: Gaussian current source $I_1 = e^{-\frac{1}{2}(\frac{T-t_0}{\sigma})^2}$ where $t_0 = 30000, T$ is the time step.

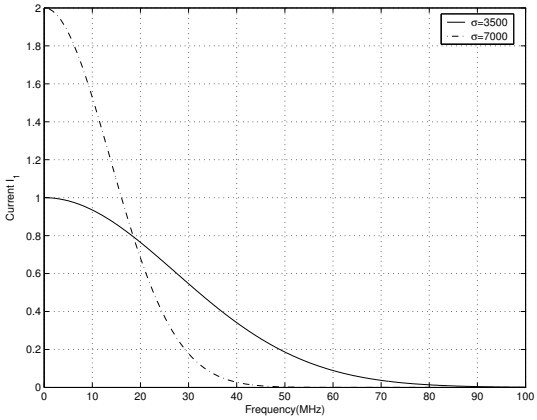

Figure 4.6: Comparison in the frequency-domain: Gaussian current source $I_1 = e^{-\frac{1}{2}(\frac{T-t_0}{\sigma})^2}$ where $t_0 = 30000, T$ is the time step.

is under $50MHz$, we choose $\sigma = 7000$ whose Gaussian pulse provides relatively little signal levels above $50MHz$. After all transients have dissipated, the resulting transient current $I_2(t)$ was Fourier Transformed. Then the equivalent current ratios I_2/I_1 at each frequency were obtained from the complex Fourier Transformations of $I_2(t)$ and $I_1(t)$. With a Gaussian source, Figure 4.7 shows acceptable results for a broad band response with a single simulation with comparison of some sinusoidal simulations. The good agreement validates the effectiveness mentioned in Section 1.3.

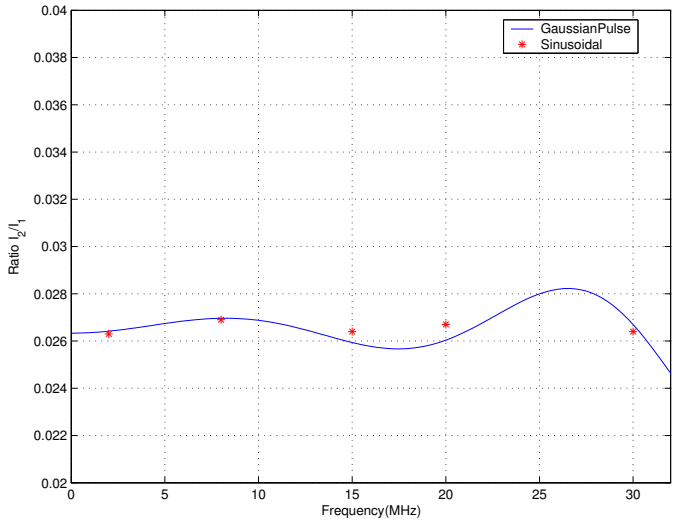

Figure 4.7: Comparison of a single simulation with Gaussian source and some sinusoidal simulations.

Chapter 5

Conclusions and Future Work

We have presented an extension of the thin-strut FDTD formalism proposed by Holland *et al.* [14] to model the coupling between primary and secondary coils in biomedical telemetry systems. Compared with the conventional FDTD method, results with the thin-strut FDTD formalism display better agreement with those obtained by the quasi-static analysis and Method of Moments.

A symmetric coupling between the field and the wire makes it possible to prove that the resulting semi-discrete field-wire system is unconditionally stable. The fully-discrete system is shown to be stable under a new stability condition together with the CFL condition. This is encouraging and lends support to the usefulness and effectiveness of further modifications of the thin-strut FDTD formalism to study multiwires running in one cell.

All the investigations so far are in free space. Given enough computer run time and computer memory, the results in the presence of the human head-eye model can be obtained. Because the human head and eyes are dispersive, it would be desirable to modify the program so that time-domain descriptions of the tissue polarization can be incorporated to account for the relaxation mechanisms that are responsible for the frequency-dependent dielectric properties. Further studies such as tissue heat absorption measured by Specified Absorption Ratio (SAR) also need to be carried out.

Bibliography

[1] P.J. Dimbyow, "Finite-difference time-domain calculations of absorbed power in the ankle for 10-100 Mhz plane wave exposure," *IEEE Trans. Biomed. Eng.,* vol. 38, pp. 423–428, 1991.

[2] N. de N. Donaldson and T.A. perkins, "Analysis of resonant coupled coils in the design of Radio Frequency Transcutaneous links," *Med. Biol. Eng. Comput.,* vol. 21, pp. 612–627, 1983.

[3] D.C. Galbraith, M. Soma and R.L. White, "A Wide-Band Efficient Inductive Transdermal Power and Data Link with Coupling Insensitive Gain," *IEEE Trans. Biomed. Eng.,* vol. BME-34, pp. 265–275, April 1987.

[4] M. Soma, D.C. Galbraith and R.L. White, "Radio-frequency Coils in Implantable Devices: Misalignment Analysis and Design Procedure," *IEEE Trans. Biomed. Eng.,* vol. BME-34, pp. 276–282, April 1987.

[5] F.C. Flack, E.D. James and D.M. Schlapp, " Mutual inductance of air-cored coils: Effect on design of RF–coupled implants," *Med. Biol. Eng.,* vol. 9, pp. 79–85, 1971.

[6] G.J. Burke and A.J. Poggio, "Numerical electromagnetic code (NEC) — method of moments," Part I, Report UCID-18834, Lawrence Livermore National Laboratory, CA, Jan. 1981.

[7] S.D. Gedney, "An anisotropic perfectly matched layer-absorbing medium for the truncation of FDTD lattices," *IEEE Trans. Antennas Propagat.,* vol. 44, no. 12, pp. 1630–1639, Dec. 1996.

[8] F.E. Terman. *Radio Engineers' Handbook.* New York: McGraw-Hill, 1943.

[9] K.S. Yee, "Numerical solution of initial boundary value problems involving Maxwell's equations in isotropic media," *IEEE Trans. Antennas Propagat.,* vol. AP-14, pp. 302–307, May 1966.

[10] S.S. Zivanovic, K.S. Yee and K.K. Mei, "A subgridding method for the time-domain finite-difference method to solve Maxwell's equations," *IEEE Trans. Microwave Theory and Tech.,* vol. 39, no. 3, pp. 471–479, Mar. 1991.

[11] S. Xiao and R. Vahldieck, "An improved 2D-FDTD algorithm for hybrid mode analysis of quasi-planar transmission lines," *Proc. 1993 MTT-S,* pp. 421–424, 1993.

[12] M.J. White, M.F. Iskander and Z.L. Huang, "Development of a multigrid FDTD code three-dimensional application," *IEEE Trans. Antennas Propagat.,* vol. AP-45, no. 10, pp. 1512–1517, Oct. 1997.

[13] K.R. Umashankar, A. Taflove and B. Beker, "Calculation and experimental validation of induced currents on coupled wires in an arbitrary shaped cavity," *IEEE Trans. Antennas Propagat.,* vol. AP-35, pp. 1248–1257, Nov. 1987.

[14] R. Holland and L. Simpson, " Finite-difference Analysis of EMP Coupling to Thin Struts and Wires," *IEEE Trans. Electromagn. Compat.,* vol. 23, pp. 88–97, 1981.

[15] J.-P. Bérenger, "A Multiwire Formalism for the FDTD Method," *IEEE Trans. Electromagn. Compat.,* vol. 42, no. 3, Aug. 2000.

[16] G.D. Smith, *Numerical solution of partial differential equations : finite difference methods,* Oxford University Press, 3rd edition, 1985.

[17] D.K. Cheng, *Field and Wave Electromagnetics,* Addison Wesley, second edition, 1989.

[18] A. Taflove and M.E. Brodwin, "Numerical solution of steady-state electromagnetic scattering problems using the time-dependent Maxwell's equations", *IEEE Trans. Microwave Theory and Tech.,* vol. MTT-23, pp. 623–630, Aug. 1975.

[19] J.P. Bérenger, "A perfectly matched layer for the absorption of electromagnetic waves," *J. Comput. Phys.,* vol. 114, pp. 185–200, 1994.

[20] K.S. Kunz and R.J. Luebbers, *The finite difference time domain method for electromagnetics,* CRC Press, 1993.

[21] K.L. Shlager and J.B. Schneider, "A survey of the finite-difference time-domain literature," *Advances in Computational Electrodynamics: The Finite-Difference Time-Domain Method,* A. Taflove, Artech House, 1998.

[22] C.M. Furse and O.P. Gandhi, "Calculation of electric fields and currents induced in a millimeter-resolution human model at 60 Hz using the FDTD method with a novel time-to-frequency-domain conversion," *Antennas and Propagation Society International Symposium,1996. AP-S. Digest ,* vol 3, pp. 1798–1801, Jul. 1996.

[23] C.M. Furse, "Faster than Fourier: ultra-efficient time-to-frequency-domain conversions for FDTD simulations", *IEEE Antennas and Propagation Magazine,* vol. 42, issue 6, pp. 24–34, Dec. 2000.

[24] A. Taflove and S.C. Hagness, *Computational Electrodynamics: The Finite-Difference Time-Domain Method,* Artech House, second edition, 2000.

[25] J.L. Meyer, D.S. Kapp, P. Fessenden, and G.H. Hahn, "Hyperthermia oncology: Current biology, physics, and clinical results," *Pharmac. Ther.,* vol. 42, pp. 251–288, 1989.

[26] J.P. Bérenger, "A multiwire formalism for the FDTD method," *IEEE Trans. Electromagn. Compat.,* vol. 42, no. 3, pp. 257-264, Aug. 2000.

[27] A. Ruddle, D. Ward, R. Scarmuzza, and V. trenkic, "Development of thin wire models in tlm," *IEEE Int. EMC Symp.,* vol. 2, pp. 196-201, Denver, CO, 1998.

[28] D.J. Riley and C.D. Turner, "The VOLMAX transient electromagnetic modeling system, including sub-cell slots and wires on random non-orthogonal cells," *14th Annual Review of Progress in Applied Computational Electrmagnetics,* vol. 2, pp. 816–824, Monterey, CA, March 1998.

[29] D.J. Riley, "Transient finite-elements for computational electrmagnetics: Hybridizaiton with finite differences, modeling thin wires and thin slots, and parallel processing," *17th Annual Review of Progress in Applied Computational Electrmagnetics,* Monterey, CA, March 2001.

[30] Z. Huang, K.R. Demarest and R.G. Plumb, "An FDTD/MoM hybrid Technique for modeling complex antennas in the presence of heterogeneous grounds", *IEEE Trans. Geoscience and Remote Sensing,* vol. 37, no. 6, Nov. 1999.

[31] M. Douglas, M. Okoniewski, and M.A. Stuchly, "Accurate modeling of thin-wire antennas in the FDTD method," *Microwave Opt. Technol. Lett.,* vol 21, no. 4, pp. 261–265, May 1999.

[32] G.G. O'Brien, M.A. Hyman, and S.A. Kaplan, "A study of the numerical solutions of partial differential equations," *J. Math. Phys.,* vol. 29, pp. 23–251, 1950.